Chemical Engineering Journal 363 (2019) 374–382

Contents lists available at ScienceDirect

Chemical Engineering Journal

journal homepage: www.elsevier.com/locate/cej

Effects of H_2O_2 generation over visible light-responsive $Bi/Bi_2O_{2-x}CO_3$ nanosheets on their photocatalytic NO_x removal performance

Yanfeng Lu[a,b,c], Yu Huang[a,b,*], Yufei Zhang[a], Tingting Huang[a], Haiwei Li[d], Jun-ji Cao[a,b], Wingkei Ho[e]

[a] Key Laboratory of Aerosol Chemistry and Physics, Institute of Earth Environment, Chinese Academy of Sciences, Xi'an 710061, China
[b] State Key Lab of Loess and Quaternary Geology (SKLLQG), Institute of Earth Environment, Chinese Academy of Sciences, Xi'an 710061, China
[c] University of Chinese Academy of Sciences, Beijing 100049, China
[d] Department of Civil and Environmental Engineering, The Hong Kong Polytechnic University, Hung Hom, Hong Kong, China
[e] Department of Science and Environmental Studies, The Hong Kong Institute of Education, Hong Kong, China

HIGHLIGHTS

- Oxygen vacancies-engineered $Bi/Bi_2O_{2-x}CO_3$ nanosheets were designed and synthesized.
- The as-prepared samples show complete oxidation of NO under visible light.
- Oxygen vacancies promoted the directional charge migration and H_2O_2 generation.
- Effects of H_2O_2 generation during the photocatalytic processes were investigated.
- The NO degradation mechanisms and biocompatibility were systematically studied.

GRAPHICAL ABSTRACT

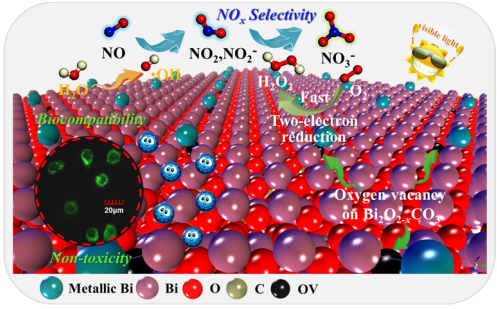

ARTICLE INFO

Keywords:
Photocatalysis
NO oxidation
Oxygen vacancy
H_2O_2
Selectivity

ABSTRACT

The photocatalytic removal of gaseous NO_x is commonly accompanied by secondary pollution, which necessitates the development of highly efficient nanostructured catalysts with a decreased propensity to toxic intermediate production. Herein, we describe the synthesis of plasmonic $Bi/Bi_2O_{2-x}CO_3$ and demonstrate the presence of surface oxygen vacancies therein, revealing that the maximal NO_x removal efficiency of $Bi/Bi_2O_{2-x}CO_3$ under visible light irradiation reached 50.5% and exceeded that of a commercial photocatalyst, while the production of toxic NO_2 as a by-product was completely suppressed (the selectivity reached up to 98%). In-situ introduction of plasmonic Bi on the surface of $Bi_2O_{2-x}CO_3$ promoted the generation of H_2O_2 by capturing electrons from the defect states of $Bi_2O_{2-x}CO_3$ via the two-electron reduction of O_2 and thus inhibited NO_2 production (as confirmed by scavenger experiments), additionally broadening the light absorption range of the above photocatalyst. Moreover, surface oxygen vacancies in Bi–O layers provided a channel for electron transfer between Bi and $Bi_2O_{2-x}CO_3$, which resulted in increased charge separation efficiency (maximum photocurrent = 1.1 μA cm^{-2}, 14.5 times higher than that of pristine $Bi_2O_2CO_3$). Furthermore, the toxicity assessment authenticated good biocompatibility of $Bi/Bi_2O_{2-x}CO_3$. Thus, this study sheds light on the possible roles of H_2O_2 in NO_x degradation and provides an efficient surface engineering strategy to prepare highly reactive and selective photocatalysts.

* Corresponding author at: Key Laboratory of Aerosol Chemistry and Physics, Institute of Earth Environment, Chinese Academy of Sciences, Xi'an 710061, China.
E-mail address: huangyu@ieecas.cn (Y. Huang).

https://doi.org/10.1016/j.cej.2019.01.172
Received 9 November 2018; Received in revised form 22 January 2019; Accepted 29 January 2019
Available online 01 February 2019

1. Introduction

One of the major challenges faced by developing countries is NO_x (NO and NO_2) pollution, which originates from the combustion of fossil fuels and poses a great threat to human health, additionally causing events such as acid rain and photochemical smog [1,2]. Although high-concentration NO_x emissions can be mitigated by several traditional technologies (selective catalytic reduction, absorption, and adsorption), the low efficiency of these techniques and their tendency to generate secondary pollutants make them poorly suited for the removal of low-concentration NO_x [3,4]. Currently, photocatalysis has been recognized as a promising technology of ppb-level NO removal [5,6], converting toxic NO_x into nitrates and thus stimulating plant growth and enhancing soil carbon storage [6,7]. However, the widespread use of photocatalytic methods is hindered by the weak redox capacity and deactivation of photocatalysts as well as by their tendency to generate substantial amounts of toxic by-products [8,9]. Thus, to be well suited for environmental remediation, NO_x removal photocatalysts should allow the highly effective transformation of NO into non-toxic species.

According to several reports, oxygen vacancies (OVs) can act as active sites and optimize the electronic band structure to facilitate the separation of electron-hole pairs and thus promote the generation of reactive oxygen species (ROS) involved in important surface reactions in heterogeneous photocatalysis [10–12]. Among the various ROS, $OH^{\cdot}$ and $O_2^{\cdot -}$ are the ones widely researched for environmental purification processes [6,13], whereas the role of H_2O_2 in heterogeneous photocatalysis is underexplored, even though this species can oxidize a broad variety of inorganic and organic substrates under very mild conditions [14–16]. Although oxides with surface OVs are capable of in situ H_2O_2 generation via O_2 activation by electrons to enhance Fenton reaction efficiency [17,18], the OV-promoted selective formation of H_2O_2 in heterogeneous photocatalysis has not been extensively investigated. Importantly, H_2O_2 can effectively and directly oxidize NO_2, which is a by-product of photocatalytic NO removal [19,20]. According to recent reports, the aqueous-phase oxidation of SO_2 by NO_2 is of critical importance for the efficient formation of sulfates accounting for the Chinese haze [21]. Therefore, the development of novel and reliable techniques of engineering oxygen vacancy-containing catalytic surfaces is indispensable for a deep understanding of the roles of H_2O_2 in heterogeneous photocatalytic reactions.

To achieve the above goal, we herein selected Bi subcarbonate ($Bi_2O_2CO_3$) [22] as a model environmentally friendly semiconductor photocatalyst. It has attracted great interest due to its interfacial $Bi_2O_2^{2+}$ and CO_3^{2-} layers therein offer great potential for the enhancement of photocatalytic activity because they can facilitate the separation of the photo-induced electron-hole pairs and thus improve the quantum yields [23]. To control the delicate surface structure of the above catalyst, we introduced metallic Bias a synergetic component to efficiently broaden the light absorption range and enhance charge migration by surface plasmon resonance (SPR) [24]. In particularly, OV-containing $Bi/Bi_2O_{2-x}CO_3$ nanosheets were prepared via in situ one-pot reduction and systematically characterized. Finally, a possible photocatalytic mechanism was proposed to study the structure-property relationships between OVs and H_2O_2 production. Thus, this study inspires the further exploration of surface engineering techniques for preparing photocatalysts with controlled reactivity and selectivity to control air pollution.

2. Experimental section

2.1. Photocatalyst preparation

All reagents were of analytical grade and used without further purification. Typically, $NaBiO_3$ (0.63 g) and urea (0.48 g) were dissolved in distilled water (5–25 mL, maintain total solvent volume at 35 mL) in a 50-mL autoclaved Teflon vessel upon 15-min stirring. An appropriate volume of ethylene glycol (EG) was subsequently added, and the resulting solution was further stirred and ultrasonicated for 3 h. The thus produced precursor suspension was heated at 180 °C for 24 h, cooled down to room temperature, and filtered. The solid product was washed with water (10 × 8 mL) and ethanol (10 × 8 mL) and dried in vacuum at 70 °C for 12 h. The as-prepared samples were denoted as B/BOC-1, B/BOC-2 and B/BOC-3 according to the volume of added EG (10, 23, and 30 mL, respectively). For comparison, we also prepared pristine $Bi_2O_2CO_3$ (BOC) and Bi. BOC was synthesized from $NaBiO_3$ and urea in the absence of EG as described above, while Bi was synthesized by dispersing $NaBiO_3$ in EG (35 mL) in the absence of distilled water and heating the obtained mixture in a 50-mL autoclaved Teflon vessel at 180 °C for 24 h. The obtained samples were washed with water (10 × 8 mL) and ethanol (10 × 8 mL) and dried in vacuum at 70 °C for 12 h.

2.2. Characterization methods

Powder X-ray diffraction (XRD; PANalytical, X'pert, the Netherlands) patterns were recorded at a scan rate of $0.04^{\circ}\,s^{-1}$ using Cu K_α (λ = 0.15406 nm) radiation. Sample morphology and structure were characterized by field-emission scanning electron microscopy (FE-SEM; Zeiss SUPRA 55, Germany) and transmission electron microscopy (TEM; JEOL JEM-2010, Japan). Surface chemical states were investigated by X-ray photoelectron spectroscopy (XPS; Thermo ESCALAB 250, USA), and binding energies were calibrated using the C1s peak of adventitious carbon at 284.6 eV. Elemental contents were determined utilizing an Elementar Vario EL instrument (Vario EL III, Germany; detection limit = 0.015%, standard deviation < 0.1% abs). Optical properties were characterized by UV–visible diffuse reflectance spectroscopy (DRS; Varian Cary 100 Scan UV–vis, USA) using $BaSO_4$ as a reference. Charge separation properties were probed by photoluminescence (PL; HITACHI F-7000, Japan) spectroscopy. Surface photovoltage spectra were recorded on a self-made apparatus comprising a monochromatic light source (500-W xenon lamp + double-prism monochromator (Hilger and Watts, D 300, UK)) and a lock-in amplifier (SR830 DSP, USA) synchronized with a light chopper (SR540, USA). The employed modulating frequencies ranged from 20 to 70 Hz, and no sample pre-treatment was used. The photovoltaic cell had an ITO–sample–ITO configuration. In situ diffuse reflectance Fourier transform infrared (FTIR) spectra (VERTEX 70, Bruker, Germany) were recorded to analyze chemical composition. An electron spin resonance (ESR; ER200-SRC, Bruker, Germany) spectrometer was used to recorded in situ ESR signals of the samples at low temperature (130 K) and to detect free radicals by dispersing solid specimens in a 50-mL DMPO solution tank (aqueous dispersion for DMPO-$OH^{\cdot}$ and methanolic dispersion for DMPO-$O_2^{\cdot -}$). A 420-nm filter was used to obtain visible light ($\lambda \geq$ 420 nm). The amount of generated H_2O_2 was determined by a 2′,7′-dichlorofluorescinassay [14]. Specifically, a 1-mL sample was incubated with 9 mL of the fluorescence reagent at 37 °C for 15 min, and the concentration of generated H_2O_2 was determined by a spectrofluorometer (USB4000-FL-450, Ocean Optics, Dunedin, USA) based on fluorescence intensity at 525 nm (excitation wavelength = 470 nm). After the photocatalytic activity test was completed, intermediates and final products (nitrate and nitrite ions) remaining on the catalyst powders were extracted by immersing the powders into deionized water (10 mL) and measured with a Dionex−600 Ion Chromatograph (Dionex Inc., Sunnyvale, CA, USA) equipped with an IonPac AS14A column. The mobile phase was composed of a mixture of 1.8 mM Na_2CO_3 and 1.7 mM $NaHCO_3$ at a flow rate of $1.20\,mL\,min^{-1}$, and the injected sample volume was 20 μL. The detection limit for NO_2^- and NO_3^- was $5\,\mu g\,L^{-1}$ and $25\,\mu g\,L^{-1}$, respectively.

2.3. In situ DRIFTS for NO conversion mechanism

All IR spectra were recorded on a VERTEX 70 spectrometer (Bruker, Germany) equipped with an in situ reaction chamber, gas system, light source, and pretreatment equipment. Prior to the adsorption process, the samples were purged by high-purity He for 1 h at 150 °C to clean the catalyst surface and then the background spectrum was collected after cooling at 30 °C. Then, the reaction gas with 30 mL min^{-1} NO (50 ppm) and 30 mL min^{-1} O_2 was sent to the reaction chamber. Under dark conditions, NO adsorption on the catalysts was carried out for 40 min. Next, photocatalysts were illuminated by a visible light source (≥420 nm) for 40 min. FTIR spectra were recorded every 2 min and the scanning range was 4000–600 cm^{-1}.

3. Results and discussion

3.1. Microstructure and chemical composition

Fig. 1a shows the XRD patterns of Bi/$Bi_2O_{2-x}CO_3$ samples, revealing the presence of peaks at 30.3° and 27.3°, which were indexed to orthorhombic $Bi_2O_2CO_3$ (PDF Card No. 84-1752)[25] and rhombohedral Bi (PDF Card No. 85-1329), respectively.[26] Additionally, the successful preparation of the above nanosheets was confirmed by FTIR spectroscopy (Fig. S1). Compared to pristine BOC, which comprised micrometer-scale plates (~2 μm, Fig. S2a and Fig. 1b), B/BOC-2 comprised numerous petal-like hierarchical nanoclusters self-assembled by nanosheets (~100 nm, Fig. S2b and Fig. 1c). High-resolution TEM (HRTEM) imaging of BOC (Fig. 1d) and B/BOC-2 (Fig. 1e) revealed the presence of two different lattice spacing (0.37 and 0.33 nm) in the latter case, corresponding to the (0 0 2) lattice plane of BOC [25] and the (1 0 2) lattice plane of Bi, respectively [27,28]. Elemental X-ray mapping (Fig. 1f–j) further demonstrated that Bi, O, and C elements were uniformly distributed in B/BOC-2 heterojunctions in view of their orientated growth promoted by EG as a solvothermal reductant. The mass contents of Bi in B/BOC-1, B/BOC-2, and B/BOC-3 were determined by elemental analysis (Table 1) and equaled 4.63, 9.66, and 17.30 wt%, respectively.

Table 1
C, $Bi_2O_2CO_3$ and Bi contents (wt%) of investigated samples determined by elemental analysis.

	B/BOC-1	B/BOC-2	B/BOC-3
C	2.24	2.12	1.94
$Bi_2O_2CO_3$	95.37	90.34	82.70
Bi	4.63	9.66	17.30

The surface chemical compositions of BOC and B/BOC-2 were probed by XPS measurements, which revealed the presence of Bi, O, and C (Fig. S3). As shown in Fig. 2a, the Bi4f XPS spectrum of BOC displayed two characteristic peaks of Bi^{3+} at 164.4 and 159.1 eV [29], while the peaks at 162.4 and 156.9 eV additionally observed in the spectrum of B/BOC-2 were ascribed to the Bi–Bi bonds of elemental Bi. In addition, the C 1s spectra of the above samples (Fig. 2b) featured two symmetric peaks at 288.3 and 284.6 eV that were assigned to the carbonate ions of BOC and carbon-containing species adsorbed on the sample surface. Notably, the intensity of the C 1s peak at 288.3 eV decreased upon the reduction of Bi^{3+} to metallic Bi on the BOC surface, and the peaks of Bi^{3+} concomitantly shifted to lower binding energy (by 0.3 eV), which was thought to reflect the preservation of electrostatic balance during the above reduction [29]. Therefore, the above mentioned transformation and the strong interaction between BOC and Bi could influence the electronic distribution in Bi–O layers, which may result in the generation of surface oxygen vacancies in the Bi–O layer for BOC.

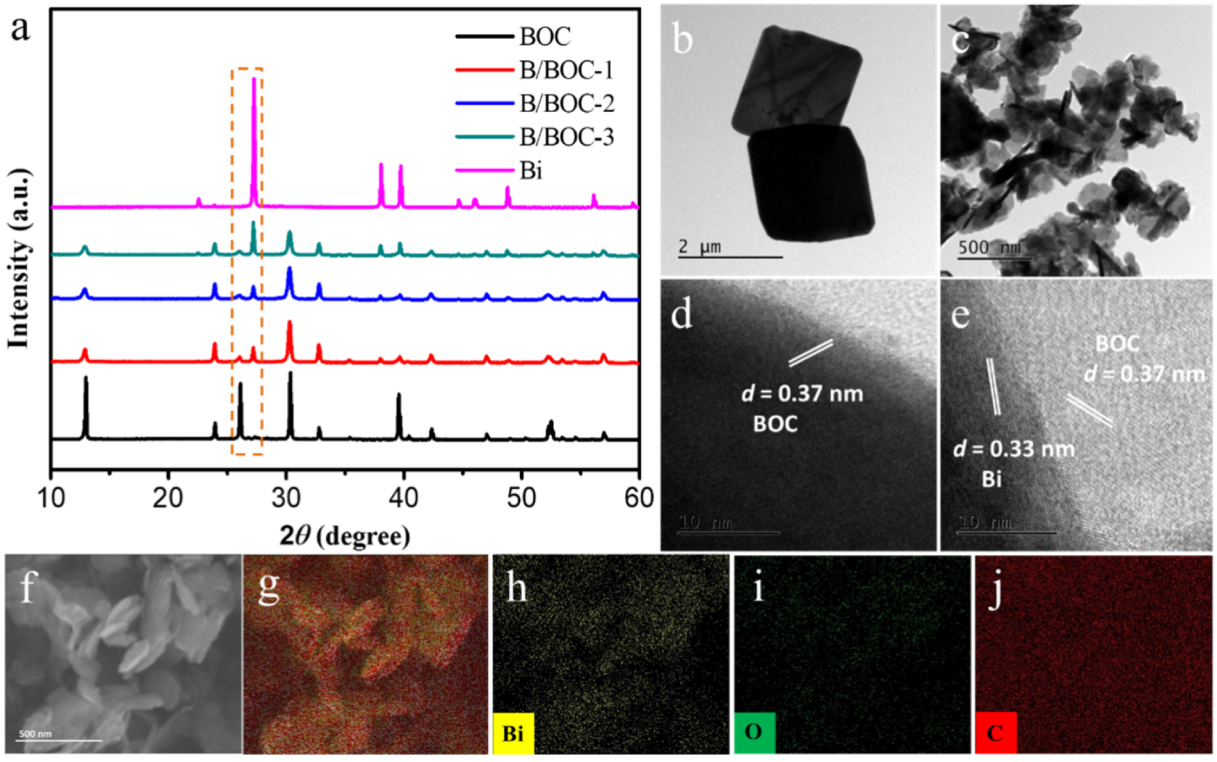

Fig. 1. (a) XRD patterns of as-prepared samples; (b, c) TEM and (d, e) HRTEM images of BOC (b, d) and B/BOC-2 (c, e); (f) SEM image of B/BOC-2 and (g–j) the corresponding elemental X-ray mappings for Bi, O and C.

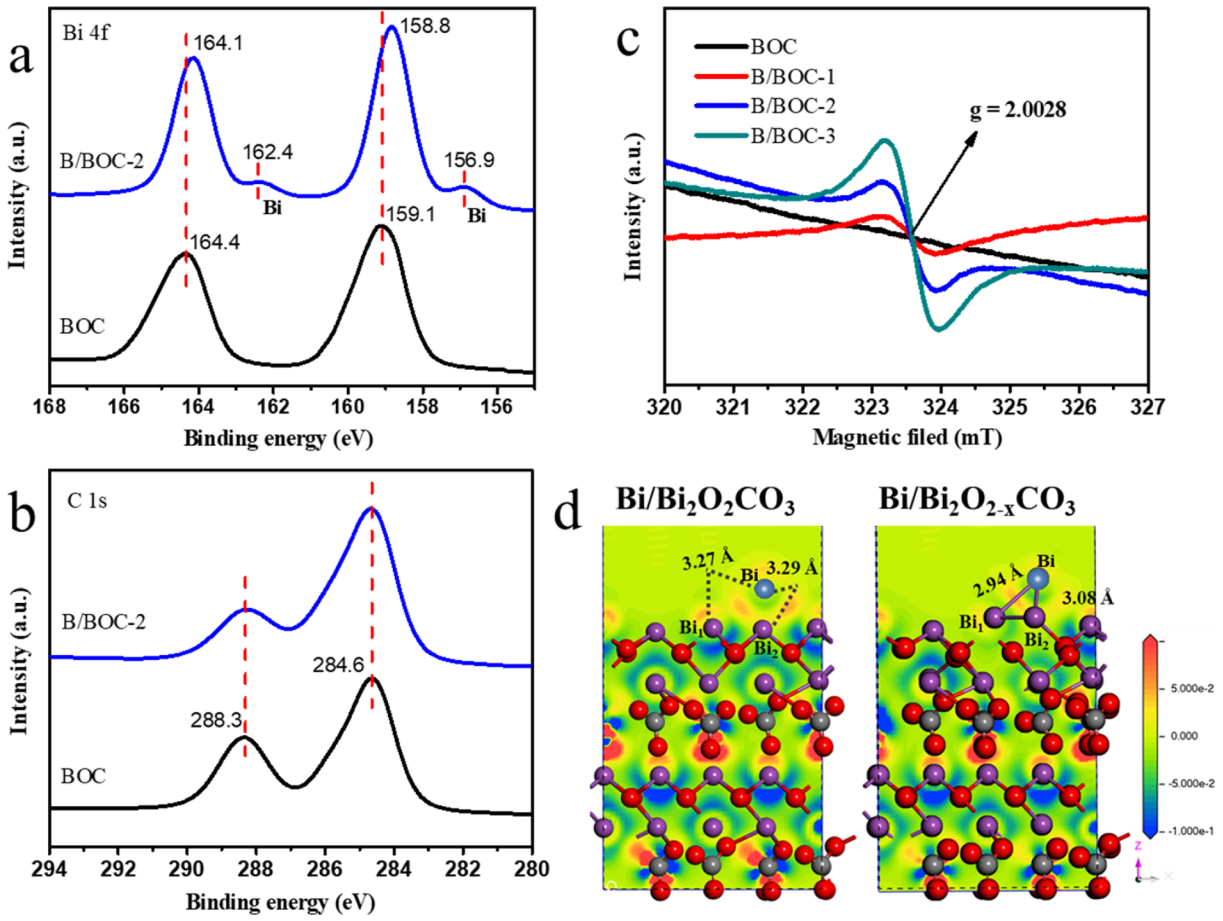

Fig. 2. High-resolution Bi 4f (a) and C 1s (b) spectra of BOC and B/BOC-2; (c) ESR spectra of BOC and B/BOC-1–3; (d) DFT-calculated crystal structure and electron density differences of all atoms in $Bi/Bi_2O_2CO_3$ and $Bi/Bi_2O_{2-x}CO_3$ systems. Charge accumulation/depletion regions are indicated by blue/red color, respectively. (For interpretation of the references to color in this figure legend, the reader is referred to the web version of this article.)

The existence of OVs was directly confirmed by ESR spectroscopy. As shown in Fig. 2c, all $Bi/Bi_2O_{2-x}CO_3$ heterojunctions showed characteristic OV signals at $g = 2.0028$, while no such signals were observed for pristine BOC [10,30]. Based on the electroneutrality condition and the fact that the concentration of OVs increased with progressing reduction of Bi^{3+} on the BOC surface, the above signals were explained by the formation of single electrons in the Bi–O layer, in agreement with XPS results [31]. Briefly, the partial reduction of Bi^{3+} on the surface of BOC led to the sputtering of some oxygen atoms from the surface Bi–O layer and the concomitant formation of OVs, resulting in "oxygen vacancy doping" (Fig. S4). The influence of OVs on the interaction between Bi and $Bi_2O_{2-x}CO_3$ was also investigated by theoretical methods (the detailed description of the density functional theory (DFT) calculation methods is available in Supporting Information), which showed that Bi on the surface of $Bi_2O_{2-x}CO_3$ exhibited a more positive charge density than that of Bi on the surface of OV-free $Bi_2O_2CO_3$ (Fig. 2d). Additionally, a new strong interaction was established between Bi–Bi_1 and Bi–Bi_2 in the $Bi/Bi_2O_{2-x}CO_3$ heterojunction. It is noticed that the extent of Bi–Bi_1 and Bi–Bi_2 reduced obviously with the bond length decreased from 3.27 Å and 3.29 Å to 2.94 Å and 3.08 Å, i.e., the presence of OVs in the surface Bi–O layer promoted the interaction between Bi and $Bi_2O_{2-x}CO_3$ and the corresponding electron transfer.

3.2. Photocatalytic activity and selectivity of $Bi/Bi_2O_{2-x}CO_3$ nanosheets

The photocatalytic activity of $Bi/Bi_2O_{2-x}CO_3$ heterojunctions under visible light irradiation was evaluated using NO_x as a model atmospheric pollutant. Fig. 3a presents the efficiencies of NO removal over as-prepared samples and a commercial P25 catalyst, demonstrating that less than 5% NO was removed over pristine BOC after 30-min irradiation. The poor performance of pristine BOC was ascribed to its wide bandgap and the large (micron-scale) size of constituent plates, which hindered the generation of photoexcited electrons and their transfer to the semiconductor surface. Conversely, B/BOC-1, B/BOC-2 and B/BOC-3 exhibited NO removal performances superior to that of P25 (16.1%), with the maximum removal efficiency (50.5% within 30 min) observed for B/BOC-2. Fig. S5 shows the NO removal efficiencies of photocatalysts obtained using different amounts of the reducing agent, revealing a similar activity trend. Thus, the above results demonstrated that the synergy between surface-plasmon-resonant Bi and surface OVs in the $Bi/Bi_2O_{2-x}CO_3$ heterojunction resulted in enhanced photocatalytic NO removal efficiency under visible light irradiation.

The accumulated amounts of NO_2^- and NO_3^- on the surfaces of the B/BOC-1 and B/BOC-2 were determined by ion chromatography (IC) method (Fig. S6). The amount of NO_3^- over B/BOC-2 is the highest, while the generation of NO_2^- is efficiently suppressed (Fig. S7). This phenomenon illustrates that most of NO was completely oxidized to NO_3^-. These results provide an accurate evidence of major NO transformation over B/BOC-2. However, if large amount of nitrate ions occupy the surface active sites, it can cause the deactivation of catalysts. Fig. 3b shows that (i) the activity (i.e., NO removal efficiency) of B/BOC-2 did not significantly decrease after five repeated cycles and (ii) the concentration of NO_2 remained constant during repeated runs. Additionally, no significant photoreactivity decrease was observed for

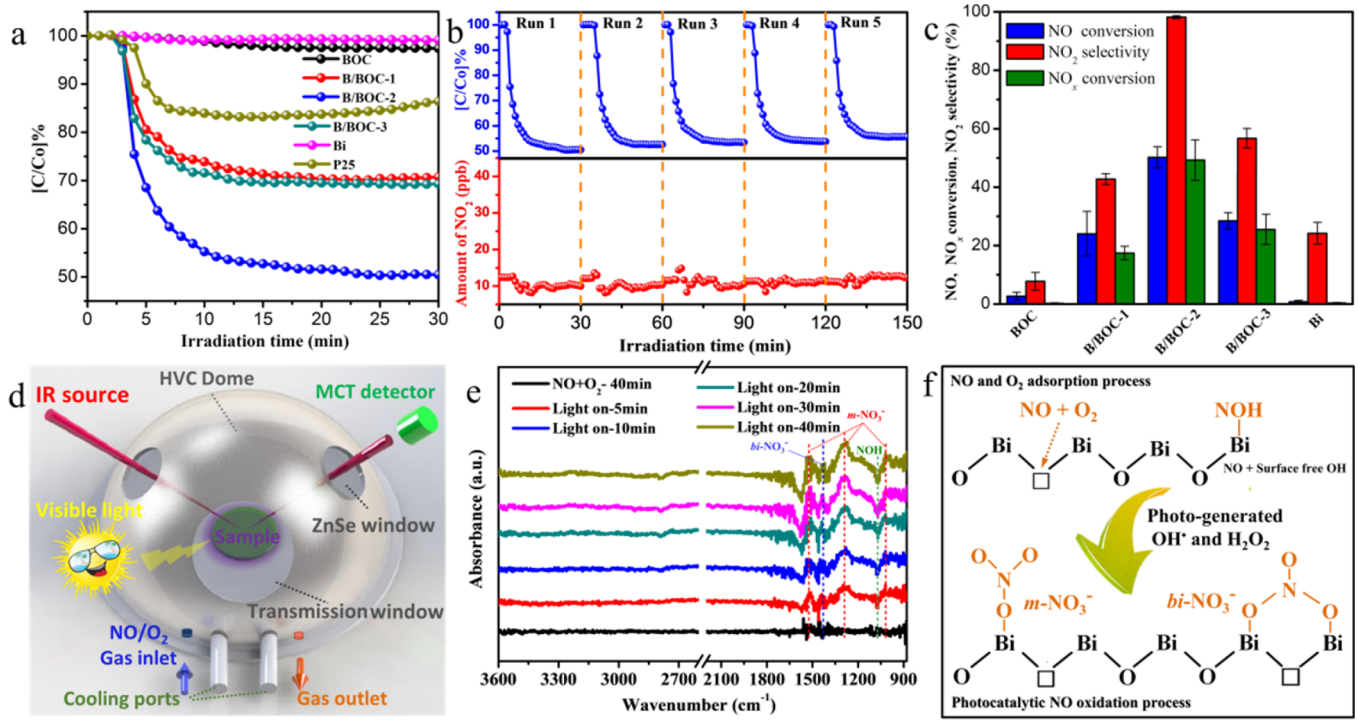

Fig. 3. (a) Photocatalytic NO removal efficiencies (C/C_o) of as-prepared samples. (b) Repeated photocatalytic removal of NO over B/BOC-2 and the amount of concomitantly produced NO_2. (c) NO, NO_x conversion and NO_2 selectivity obtained for catalysts subjected to 30-min irradiation. Error bars were calculated based on the results of several measurements using multiple catalyst batches. (d) Schematic illustration of the reaction cell for in situ FTIR study. (e) FTIR spectra recorded during photocatalytic NO oxidation over B/BOC-2. (f) Mechanism of photocatalytic NO oxidation on $Bi/Bi_2O_{2-x}CO_3$ samples.

successive runs lasting 300 min (Fig. S8). The results implied surface OVs-induced $Bi/Bi_2O_{2-x}CO_3$ heterojunction maintained the photocatalytic NO removal efficiency and inhibited the deactivation of catalysts under visible light irradiation.

Additionally, we investigated the selectivity of NO_2 production during the photocatalytic reaction, probing the relative change of NO conversion, NO_2 selectivity, and NO_x conversion over various samples (Fig. 3c). The selectivity of NO_2 over B/BOC-2 exceeded that over B/BOC-1 (43%) and B/BOC-3 (57%) by a factor of almost two, and the highest NO_2 selectivity (up to 99%) was observed for B/BOC-2. The concentration of NO over B/BOC-2 decreased from 409 to 205 ppb after 10-min irradiation with visible light (Fig. S9). More interestingly, the concentrations of NO_2 did not change during the irradiation time following the concentration change of NO. These results illustrated that the presence of OVs in $Bi/Bi_2O_{2-x}CO_3$ not only suppressed catalyst deactivation but also effectively inhibited the formation of NO_2 as a by-product. The mechanism of photocatalytic NO_x oxidation was further clarified by studying the visible light–driven catalytic removal of NO_2 and monitoring the transformations of the corresponding reaction intermediates over the photocatalyst surface (Fig. S10). Based on the obtained results, the suppression of NO_2 formation over B/BOC-2 was ascribed to the sufficient diffusion of NO_2 on the photocatalyst surface and the effective generation of reactive oxygen species for the deep oxidation of NO_2.

To directly visualize processes occurring during the photocatalytic oxidation of NO on $Bi/Bi_2O_{2-x}CO_3$ nanosheets, the change of functional groups on the sample surface under visible light irradiation was monitored by FTIR spectroscopy in a special reaction cell (Fig. 3d). First, the band at 1570, 1460 and 1070 cm^{-1} gradually decreased and became negative with increasing irradiation time (Fig. 3e). The band at 1070 cm^{-1} could be attributed to NOH and at 1570 and 1460 cm^{-1} due to NO absorption species, suggesting the disproportionation of NO on the surface of $Bi/Bi_2O_{2-x}CO_3$ [32]. Seconds, replaced NO was immediately converted to other nitro compounds. The sharp bands at 1520, 1290 and 1020 cm^{-1} were assigned to nitrate in a particular monodentate state and 1440 cm^{-1} was ascribed to the almost symmetrical surface bidentate nitrate [33,34]. These bands gradually gained intensity as the irradiation time increased from 0 to 40 min, which strongly suggested that surface OV–containing $Bi/Bi_2O_{2-x}CO_3$ could deeply oxidize NO to NO_3^- (Fig. 3f). The nitrogen mass balance was also calculated to verify the quantitative transformation of NO into nitrite or nitrate. As shown in Fig. S11, the B/BOC-2 shows the maximum amount in NO conversion and accumulation of NO_3^- with lower NO_2 and NO_2^- yield, which is consistent with the results of FTIR. Compared with the calculated values, the measured values are lower due to the particle phase of nitrates drawn airflow away or some new species undetectable by chemiluminescent NO*x* analyzer and ion chromatography (the inserted Table S1). The results of nitrogen mass balance illustrate the $Bi/Bi_2O_{2-x}CO_3$ heterojunction with surface OV–containing could potentially generate more reactive oxygen species for the deep oxidation leading to complete oxidation of NO.

3.3. Charge transfer and optical properties

The effect of surface OVs in $Bi/Bi_2O_{2-x}CO_3$ heterojunctions on the electron-hole separation efficiency was investigated by transient photocurrent and PL measurements. Fig. 4a shows that all samples quickly responded to visible light irradiation. Generally, high photocurrent density is indicative of rapid photogenerated charge transfer and high separation efficiency.[8] Fig. 4a shows that B/BOC-2 exhibited the highest charge separation and transfer efficiency (1.1 μA cm^{-2}, 14.5 times higher than that of BOC). Thus, OVs were concluded to govern visible light response and ultrafast charge transfer [35], i.e., OV-rich $Bi/Bi_2O_{2-x}CO_3$ heterojunctions showed increased photocatalytic activity. However, excessive reduction of Bi^{3+} resulted in a high concentration of OVs (Fig. 2c) that acted as charge carrier recombination centers.[36] Similar results were obtained by PL spectroscopy (Fig. 4b), i.e., the strong emission of B/BOC-3 infers from the deep OVs to

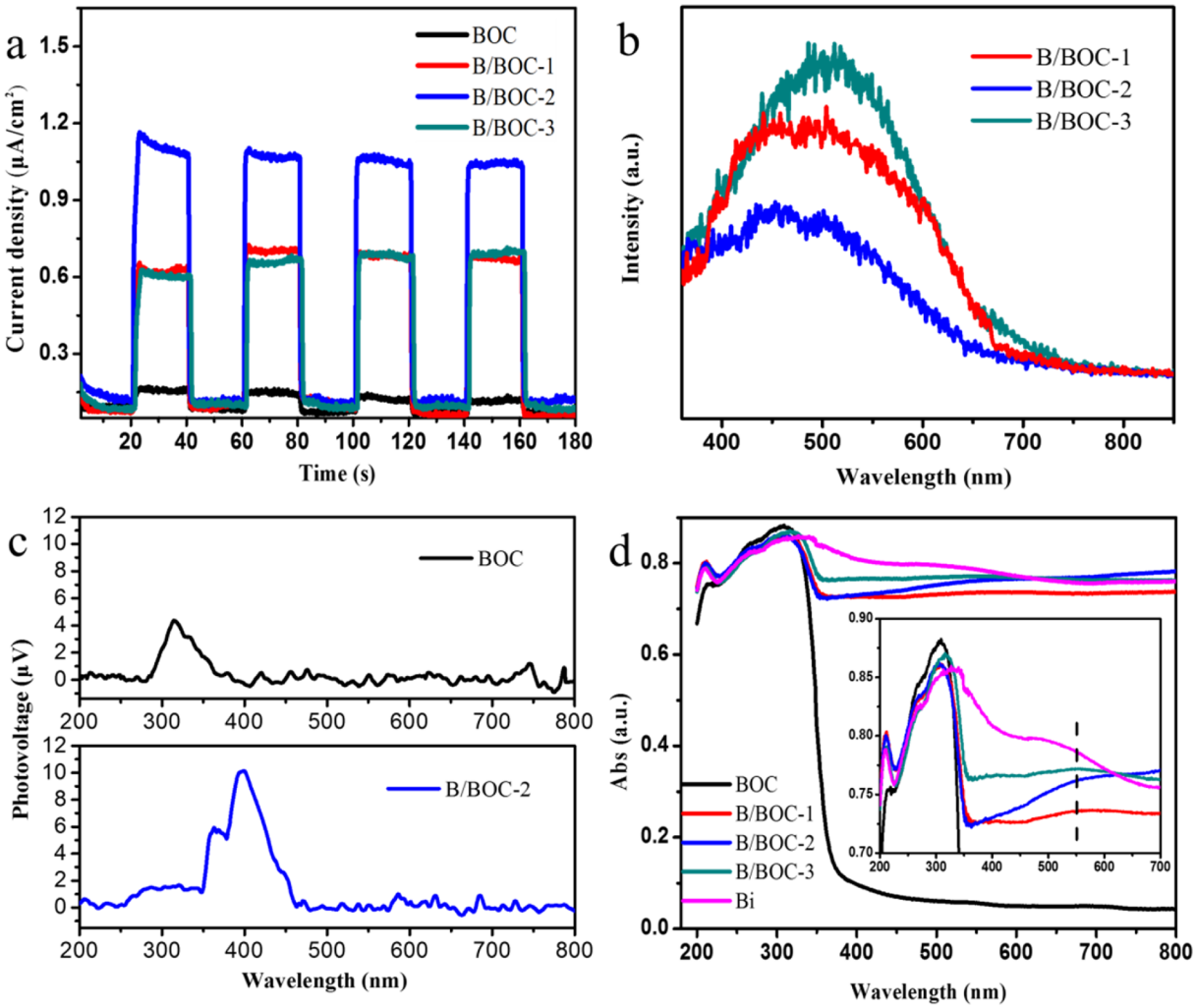

Fig. 4. (a) Photocurrent responses of fabricated samples in 0.5 M Na_2SO_4 under visible light irradiation (λ = 420 nm); (b) room-temperature PL spectra of B/BOC samples; (c) surface photovoltage spectra of BOC and B/BOC-2; (d) UV–vis DRS spectra of Bi, BOC and B/BOCs.

increase new recombination center [10,17]. Meanwhile, B/BOC-2 exhibited the weakest emission peak, which, together with the results of transient photocurrent measurements (Fig. 4a), indicated that this sample exhibited the most pronounced ability to inhibit the recombination of electron-hole pairs. Therefore, OVs were concluded to be responsible for the improvement of carrier separation efficiency.

The mechanism of photogenerated electron transfer in Bi/$Bi_2O_{2-x}CO_3$ nanosheets was probed by surface photovoltage spectroscopy (SPS). Fig. 4c shows surface photovoltage spectra of BOC and B/BOC-2, demonstrating that a strong response peak at ~280 to 370 nm (UV region) was observed in the former case [37]. In the case of B/BOC-2, the above signal gained intensity and shifted to longer wavelengths, which was ascribed to the increased efficiency of electron-hole pair separation [38]. Moreover, the strong SPS signals at 380–480 nm probably reflected the migration of plasmonic electrons from metallic Bi to $Bi_2O_{2-x}CO_3$ [38–40]. These results demonstrated the existence of a strong interaction and efficient electron transport between plasmonic Bi metal and OV-containing $Bi_2O_{2-x}CO_3$, which promoted charge transfer. SPS and photoelectrochemical analysis revealed that surface OVs in Bi–O layers can provide a channel for electron transfer between Bi and $Bi_2O_{2-x}CO_3$, allowing the transfer of electrons between defect levels and metallic Bi and thereby facilitating charge separation.

The optical properties of samples were probed by UV–vis DRS. Fig. 4d shows that Bi/$Bi_2O_{2-x}CO_3$ nanosheets exhibited a markedly extended light harvesting range extending from UV to near-infrared regions.[30] Compared to pristine BOC (3.32 eV), B/BOC-1, B/BOC-2 and B/BOC-3 exhibited decreased band gap energies (estimated from threshold wavelengths as 2.50, 2.52 and 2.42 eV, respectively) and could therefore efficiently utilize visible light.[41] Moreover, an additional wide absorption peak at ~500 nm assigned to the typical characteristic SPR of metallic Bi was observed for Bi/$Bi_2O_{2-x}CO_3$ (inset in Fig. 4d) [28,26]. This behavior was attributed to the collective excitation of free electrons in Bi metal that generated a strong resonant optical absorption with near-field and scattering enhancements [42]. The enhanced visible light adsorption ability of Bi/$Bi_2O_{2-x}CO_3$ nanosheets was assigned to the plasmonic effect of Bi metal, which verified the presence of Bi in Bi/$Bi_2O_{2-x}CO_3$ nanosheets and was consistent with the results of high-resolution TEM imaging and XPS.

3.4. Identification of ROS and the role of H_2O_2 in NO_x conversion

To elucidate the interaction mechanism between gas-phase NO_x and the photocatalyst surface, the ROS involved in photocatalytic NO_x removal over Bi/$Bi_2O_{2-x}CO_3$ were identified using ESR spectroscopy [43]. Fig. 5a displays that under the same conditions, DMPO−$OH^{\cdot}$ signals were detected only for Bi/$Bi_2O_{2-x}CO_3$ but not for BOC. Meanwhile, the production of $O_2^{\cdot -}$ was inhibited in the Bi/$Bi_2O_{2-x}CO_3$ system under visible light irradiation. Fig. 5b shows that during the photocatalytic process, H_2O_2 was generated in the Bi/$Bi_2O_{2-x}CO_3$ system but not in the pristine BOC system (as determined by the 2′,7′-

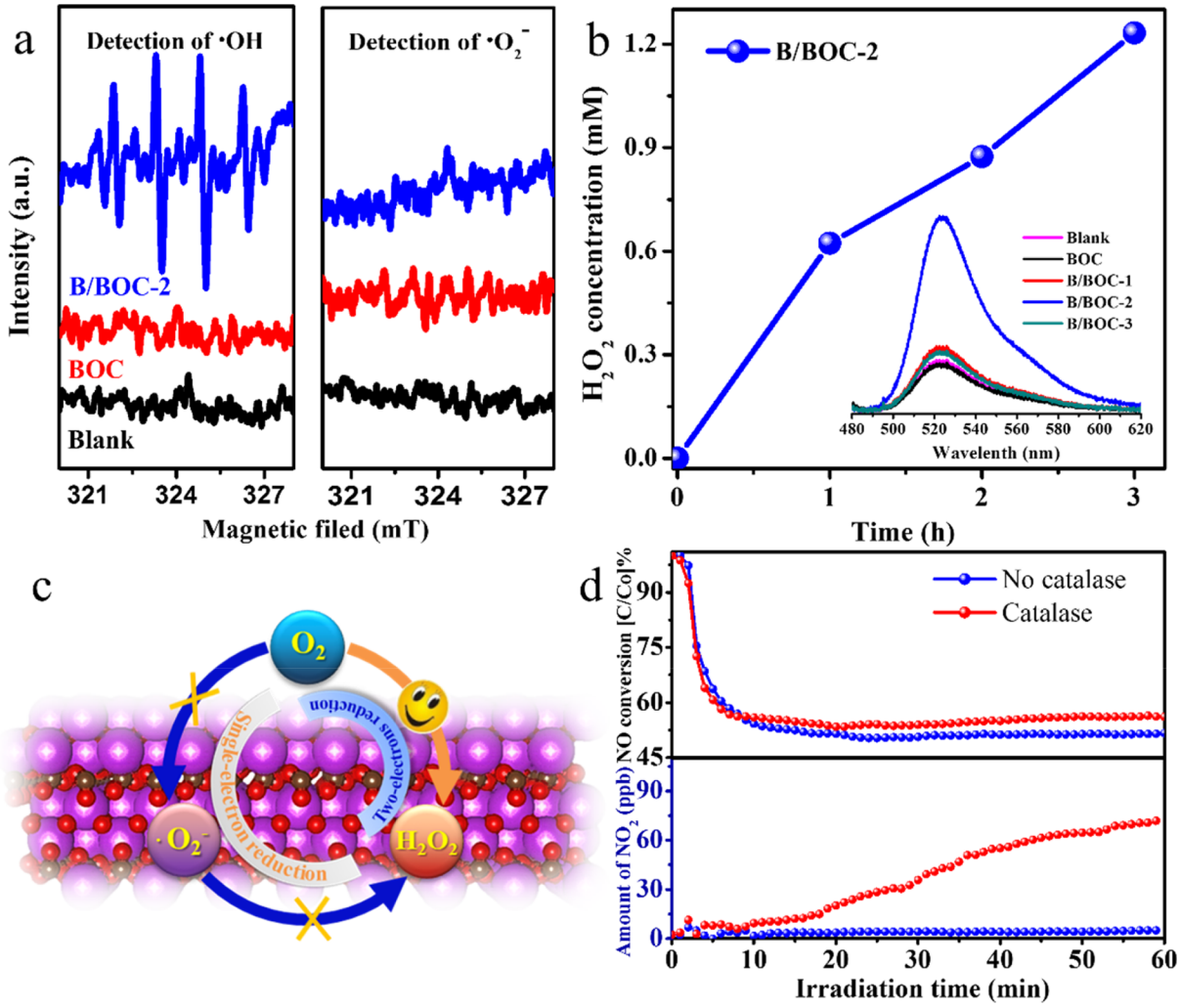

Fig. 5. (a) Detection of $OH^{\cdot}$ and $O_2^{\cdot -}$ radicals over BOC and B/BOC-2 under visible-light illumination ($\lambda \geq 420$ nm) by DMPO ESR spin trapping; (b) concentration of H_2O_2 as function of irradiation time in the B/BOC-2 system (inset: fluorescence intensities in different systems used to assay the concentration of generated H_2O_2); (c) possible mechanisms of H_2O_2 formation over $Bi/Bi_2O_{2-x}CO_3$ nanosheets; (d) influence of catalase on photocatalytic NO conversion over B/BOC-2 and the concentration of concomitantly generated NO_2 under identical conditions.

dichlorofluorescin assay) [14]. The amount of H_2O_2 generated in the B/BOC-2 system increased with increasing reaction time, which illustrated that OV-containing $Bi/Bi_2O_{2-x}CO_3$ effectively promoted the photoreduction of O_2 to H_2O_2 [14]. However, the H_2O_2 production abilities of B/BOC-1 and B/BOC-3 were dramatically lower than that of B/BOC-2, which was ascribed to the uneven distribution of Bi on the surface of the first two heterojunctions (Fig. S12). Thus, the insufficient interfacial interaction between Bi and surface OVs in B/BOC-1 and B/BOC-3 suppressed the two-electron reduction of O_2 to H_2O_2 and/or aggravated the dissociation of H_2O_2 into $OH^{\cdot}$, which resulted in rapid H_2O_2 reduction [44]. Therefore, the dissociation of H_2O_2 was concluded to be interdicted by the in situ formation of Bi, which suppressed the single-electron reduction of H_2O_2 to $OH^{\cdot}$ and enhanced the selectivity of O_2 reduction to H_2O_2. Fig. 5a shows that no characteristic peaks of DMPO-$O_2^{\cdot -}$ could be observed in the $Bi/Bi_2O_{2-x}CO_3$ system. Based on these observations, we concluded that H_2O_2 in the $Bi/Bi_2O_{2-x}CO_3$ system is mainly produced via one-step two-electron reduction of O_2 (Fig. 5c). The $Bi/Bi_2O_{2-x}CO_3$ heterojunction can facilitate the formation of H_2O_2 by in situ reduction Bi realizing the modification of OVs on the surface. The significant difference in ROS generation implied that OVs changed the transfer pathway of photoelectrons, as verified by the results of transient photocurrent measurements and SPS.

Based on the above results, the yield of H_2O_2 (and hence, the NO_2 selectivity) over B/BOC-2 was concluded to exceed that over B/BOC-1 and B/BOC-3. The relevance of H_2O_2 and NO_2 selectivity was highlighted by performing control experiments to further investigate the effect of H_2O_2 on NO_x conversion using catalase as an H_2O_2 scavenger (Fig. 5d) [20]. H_2O_2 can yield $OH^{\cdot}$ upon single-electron reduction ($H_2O_2 + e^- \rightarrow OH^- + OH^{\cdot}$) [45]. At constant visible light irradiation time, the amount of NO_2 produced during NO removal dramatically increased in the presence of catalase, which suggested that the presence of OVs in $Bi/Bi_2O_{2-x}CO_3$ is critical to H_2O_2 production selectivity. This phenomenon illustrated that the gradually reduction in photocatalytic activity and selectivity after several minutes can be aroused without H_2O_2 production due to the accumulation of the intermediates and final products occupying the active sites (Fig. 5d). In other words, the modifying of OVs can further transform NO_2 to NO_3^- at a different location due to the surface oxygen vacancy diffusion mechanism, which can alleviate the deactivation to photocatalyst. These results demonstrated that the formation of OVs via in situ reduction of Bi^{3+} on the BOC surface promoted the formation of H_2O_2 in the B/BOC-2 system to effectively and directly inhibit NO_2 formation.

Fig. 6 shows the proposed mechanisms of charge transfer and photocatalytic NO_x oxidation over $Bi/Bi_2O_{2-x}CO_3$ nanosheets. Notably, the broad band gap (3.32 eV) of pristine $Bi_2O_2CO_3$ precluded its excitation by visible light. However, the formation of a heterointerface

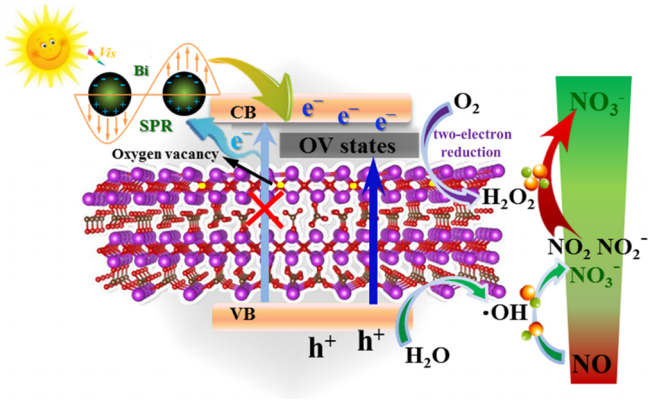

Fig. 6. Schematic illustration of charge transfer in the $Bi/Bi_2O_{2-x}CO_3$ system and the possible mechanism of photocatalysis.

between metallic Bi and $Bi_2O_{2-x}CO_3$ resulted in direct contact. The free electrons produced from metallic Bi with SPR function under visible-light irradiation, which is more prone to transfer to $Bi_2O_{2-x}CO_3$ [8,46]. Additionally, the photogenerated electrons in $Bi/Bi_2O_{2-x}CO_3$ could be excited to OV-induced defect states, and the restructured holes accumulated in the valence band of $Bi_2O_{2-x}CO_3$ and oxidized H_2O to $OH^{\cdot}$ (Eqs. (1) and (2)) [8]. The thus produced $OH^{\cdot}$ effectively oxidized NO to NO_2^-/NO_3^-, although partial conversion to NO_2 was also observed (Eqs. (3)–(5)). As expected, OVs promoted the conversion of NO_2 and NO_2^- to NO_3^- by facilitating the production of H_2O_2, which also alleviated photocatalyst deactivation (Fig. 5d). Considering the fact that adsorbed O_2 can capture electrons from the defect states of $Bi_2O_{2-x}CO_3$ to generate H_2O_2 via two-electron reduction, it is essential to facilitate the role of H_2O_2 species in deep oxidization of NO (Eqs. (6)–(8)) [16]. Therefore, the presence of OVs in $Bi/Bi_2O_{2-x}CO_3$ significantly promoted the directional transfer of photogenerated charges and activated the H_2O_2 generation pathway to facilitate deep NO_x oxidation (verified by FTIR, Fig. 3e). On the whole, the incorporation of Bi improved the light-harvesting ability of $Bi_2O_{2-x}CO_3$ ranging from UV to near-infrared light, which enhances the production of more active electrons and holes on $Bi_2O_{2-x}CO_3$ surface. Moreover, the abundant OVs in $Bi/Bi_2O_{2-x}CO_3$ system also can supply adsorption and active sites to improve visible light activity of semiconductor photocatalyst in addition to generating sufficient photo-induced electrons through two effective ways:

$$Bi/Bi_2O_{2-x}CO_3 + \text{visible light} \rightarrow e^- + h^+ \quad (1)$$

$$h^+ + OH^- \rightarrow OH^{\cdot} \quad (2)$$

$$NO + OH^{\cdot} \rightarrow NO_2^- + H^+ \quad (3)$$

$$NO + 2OH^{\cdot} \rightarrow NO_2 + H_2O \quad (4)$$

$$NO_2 + OH^{\cdot} \rightarrow NO_3^- + H^+ \quad (5)$$

$$2e^- + O_2 + 2H^+ \rightarrow H_2O_2 \quad (6)$$

$$NO_2^- + H_2O_2 \rightarrow NO_3^- + H_2O \quad (7)$$

$$2NO_2 + H_2O_2 \rightarrow 2NO_3^- + 2H^+ \quad (8)$$

3.5. Cytotoxicity assessment and fluorescence cellular imaging

The toxicity of catalyst is important for practical applications. The MTT cell viability assay was performed over different concentrations of $Bi/Bi_2O_{2-x}CO_3$ and P25 on A549 cells shown in Fig. 7a. For commercial photocatalyst P25, the cell viabilities decreased with the enhancement of P25 concentration. Cells exposed to 50 μg mL^{-1} P25 exhibited 20% reduction, and greater than 60% was observed at high concentrations of 200 μg mL^{-1} in a concentration-dependent manner. In contrast, any significant change of cell viability did not appeared treated with the supernatant of $Bi/Bi_2O_{2-x}CO_3$ at 0–200 μg mL^{-1}, indicating that $Bi/Bi_2O_{2-x}CO_3$ exhibits nontoxicity and good biocompatibility for A549 cells.

Fluorescence images were recorded to reflect cellular uptake and deformation. From the images of Fig. 7b-c, fluorescence could be observed clearly on A549 cells incubated with $Bi/Bi_2O_{2-x}CO_3$, demonstrating the good biocompatibility of $Bi/Bi_2O_{2-x}CO_3$ to penetrate the cell walls. But dimmest fluorescence of cell nucleus indicating $Bi/Bi_2O_{2-x}CO_3$ did not enter cell nucleus and generate cytotoxicity. However, no fluorescence can be observed in the cells incubated with P25 (Fig. 7d-e) under the same conditions. The microscopic observations from bright-field image reveal the good biocompatibility and nontoxicity of $Bi/Bi_2O_{2-x}CO_3$, which fall in line with the previous MTT assay.

4. Conclusion

In summary, the plasmonic $Bi/Bi_2O_{2-x}CO_3$ nanosheets with surface oxygen vacancies were successfully prepared via an in situ one-pot reduction method and the as-prepared samples were systematically characterized. The photocatalytic activity, NO_2 selectivity and stable performance under visible light irradiation were remarkably enhanced due to the in-situ introduction of plasmonic Bi on the surface of $Bi_2O_{2-x}CO_3$. The maximal efficiency of NO_x removal over $Bi/Bi_2O_{2-x}CO_3$ under visible light irradiation was significantly improved. More importantly, the production of toxic NO_2 as a by-product was completely suppressed. The generation of H_2O_2 promoted the complete oxidation of NO by capturing electrons from the defect states of $Bi_2O_{2-x}CO_3$ via the two-electron reduction of O_2. Moreover, surface oxygen vacancies in Bi–O layers provided a channel for electron transfer between Bi and $Bi_2O_{2-x}CO_3$, resulting in increasing charge separation efficiency. The as-prepared $Bi/Bi_2O_{2-x}CO_3$ samples show excellent biological compatibility as evaluated by human lung cells test. This study provides an efficient surface engineering strategy to prepare highly reactive and selective photocatalysts for air purification.

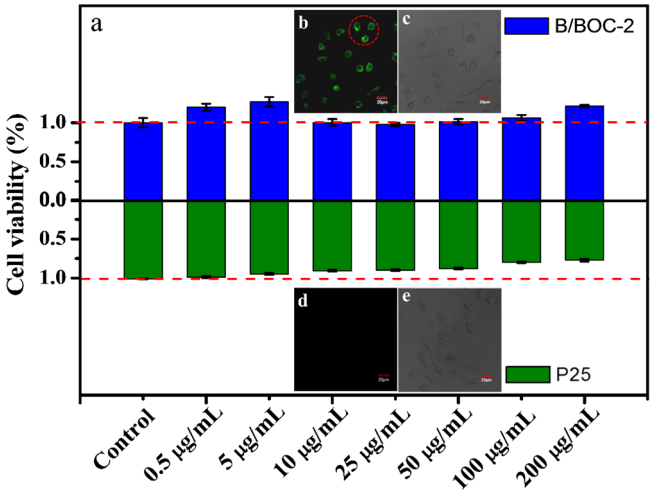

Fig. 7. Relative viability of A549 cells after incubation of 24 h with different concentration of P25 and B/BOC-2 (a); Intracellular delivery of P25 and B/BOC-2 under bright field and at an excitation wavelength of 488 nm (b-e).

Acknowledgments

This research was financially supported by the National Key Research and Development Program of China (2016YFA0203000 and 2017YFC0212200) and the National Science Foundation of China (No. 41573138 and No. 51878644). Moreover, we acknowledge the partial support by the Key Research and Development Program of Shaanxi Province (No. 2018ZDCXL-SF-02-04). Yu Huang was also supported by the "Hundred Talent Program" of the Chinese Academy of Sciences.

Appendix A. Supplementary data

Supplementary data to this article can be found online at https://doi.org/10.1016/j.cej.2019.01.172.

References

[1] H. Chen, C.E. Nanayakkara, V.H. Grassian, Titanium dioxide photocatalysis in atmospheric chemistry, Chem. Rev. 112 (2012) 5919–5948.
[2] R.J. Huang, Y.L. Zhang, C. Bozzetti, K.F. Ho, J.J. Cao, Y.M. Han, K.R. Daellenbach, J.G. Slowik, S.M. Platt, F. Canonaco, P. Zotter, R. Wolf, S.M. Pieber, E.A. Bruns, M. Crippa, G. Ciarelli, A. Piazzalunga, M. Schwikowski, G. Abbaszade, J.S. Kreis, R. Zimmermann, Z.S. An, S. Szidat, U. Baltensperger, I. El Haddad, A.S.H. Prevot, High secondary aerosol contribution to particulate pollution during haze events in China, Nature 514 (2014) 218–222.
[3] C. Misra, C. Ruehl, J. Collins, D. Chernich, J. Herner, In-use NO_x emissions from diesel and liquefied natural gas refuse trucks equipped with SCR and TWC, respectively, Environ. Sci. Technol. 51 (2017) 6981–6989.
[4] M. Seneque, F. Can, D. Duprez, X. Courtois, NO_x selective catalytic reduction (NO_x-SCR) by urea: evidence of the reactivity of HNCO, including a specific reaction pathway for NO_x reduction involving NO + NO_2, ACS Catal. 6 (2016) 4064–4067.
[5] G. Dong, D.L. Jacobs, L. Zang, C. Wang, Carbon vacancy regulated photoreduction of NO to N_2 over ultrathin g-C_3N_4 nanosheets, Appl. Catal. B 218 (2017) 515–524.
[6] H. Wang, Y. Sun, G. Jiang, Y. Zhang, H. Huang, Z. Wu, S.C. Lee, F. Dong, Unraveling the mechanisms of visible light photocatalytic NO purification on earth-abundant insulator-based core-shell heterojunctions, Environ. Sci. Technol. 52 (2018) 1479–1487.
[7] J.C. Neff, A.R. Townsend, G. Gleixner, S.J. Lehman, J. Turnbull, W.D. Bowman, variable effects of nitrogen additions on the stability and turnover of soil carbon, Nature 419 (2002) 915–917.
[8] M. Chen, J. Yao, Y. Huang, H. Gong, W. Chu, Enhanced photocatalytic degradation of ciprofloxacin over Bi_2O_3/$(BiO)_2CO_3$ heterojunctions: efficiency, kinetics, pathways, mechanisms and toxicity evaluation, Chem. Eng. J. 334 (2018) 453–461.
[9] Y. Huang, P. Wang, Z. Wang, Y. Rao, J.J. Cao, W. Ho, S.C. Lee, Protonated g-C_3N_4/Ti^{3+} self-doped TiO_2 nanocomposite films: room-temperature preparation, hydrophilicity, and application for photocatalytic NO_x removal, Appl. Catal. B 240 (2018) 122–131.
[10] C. Liu, A.Y. Zhang, D.N. Pei, H.Q. Yu, Efficient electrochemical reduction of nitrobenzene by defect engineered TiO_{2-x} single crystals, Environ. Sci. Technol. 50 (2016) 5234–5242.
[11] H. Li, J. Shang, Z. Ai, L. Zhang, Efficient visible light nitrogen fixation with BiOBr nanosheets of oxygen vacancies on the exposed 001 facets, J. Am. Chem. Soc. 137 (2015) 6393–6399.
[12] Y. Lu, Y. Huang, Y. Zhang, J.J. Cao, H. Li, C. Bian, S.C. Lee, Oxygen vacancy engineering of Bi_2O_3/$Bi_2O_2CO_3$ heterojunctions: implications of the interfacial charge transfer, NO adsorption and removal, Appl. Catal., B 231 (2018) 357–367.
[13] Y. Huang, Y. Liang, Y. Rao, D. Zhu, J.J. Cao, Z. Shen, W. Ho, S.C. Lee, Environment-friendly carbon quantum dots/$ZnFe_2O_4$ photocatalysts: characterization, biocompatibility, and mechanisms for NO removal, Environ. Sci. Technol. 51 (2017) 2924–2933.
[14] L. Wang, M. Cao, Z. Ai, L. Zhang, Dramatically enhanced aerobic atrazine degradation with Fe@Fe_2O_3 core-shell nanowires by tetrapolyphosphate, Environ. Sci. Technol. 48 (2014) 3354–3362.
[15] Y. Qin, F. Song, Z. Ai, P. Zhang, L. Zhang, Protocatechuic acid promoted alachlor degradation in Fe(III)/H_2O_2 Fenton system, Environ. Sci. Technol. 49 (2015) 7948–7956.
[16] A.D. Bokare, W. Choi, Review of iron-free Fenton-like systems for activating H_2O_2 in advanced oxidation processes, J. Hazard. Mater. 275 (2014) 121–135.
[17] H. Li, J. Shang, Z. Yang, W. Shen, Z. Ai, L. Zhang, Oxygen vacancy associated surface fenton chemistry: surface structure dependent hydroxyl radicals generation and substrate dependent reactivity, Environ. Sci. Technol. 51 (2017) 5685–5694.
[18] A.D. Bokare, W. Choi, Bicarbonate-induced activation of H_2O_2 for metal-free oxidative desulfurization, J. Hazard. Mater. 304 (2016) 313–319.
[19] S. Li, G. Dong, R. Hailili, L. Yang, Y. Li, F. Wang, Y. Zeng, C. Wang, Effective photocatalytic H_2O_2 production under visible light irradiation at g-C_3N_4 modulated by carbon vacancies, Appl. Catal., B 190 (2016) 26–35.
[20] G. Dong, L. Yang, F. Wang, L. Zang, C. Wang, Removal of nitric oxide through visible light photocatalysis by g-C_3N_4 modified with perylene imides, ACS Catal. 6 (2016) 6511–6519.
[21] G. Wang, R. Zhang, M.E. Gomez, L. Yang, M.L. Zamora, M. Hu, Y. Lin, J. Peng, S. Guo, J. Meng, J. Li, C. Cheng, T. Hu, Y. Ren, Y. Wang, J. Gao, J. Cao, Z. An, W. Zhou, G. Li, J. Wang, P. Tian, W. Marrero-Ortiz, J. Secrest, Z. Du, J. Zheng, D. Shang, L. Zeng, M. Shao, W. Wang, Y. Huang, Y. Wang, Y. Zhu, Y. Li, J. Hu, B. Pan, L. Cai, Y. Cheng, Y. Ji, F. Zhang, D. Rosenfeld, P.S. Liss, R.A. Duce, C.E. Kolb, M.J. Molina, Persistent Sulfate Formation from London Fog to Chinese Haze, PNAS 113 (2016) 13630–13635.
[22] Z. Ni, Y. Sun, Y. Zhang, F. Dong, Fabrication, modification and application of $(BiO)_2CO_3$-based photocatalysts: a review, Appl. Surf. Sci. 365 (2016) 314–335.
[23] C. Greaves, S.K. Blower, Structural relationships between $Bi_2O_2CO_3$ and β-Bi_2O_3, Mater. Res. Bull. 23 (1988) 1001–1008.
[24] J. Kim, D.M. Satoca, W. Choi, Simultaneous production of hydrogen with the degradation of organic pollutants using TiO_2 photocatalyst modified with dual surface components, Energy Environ. Sci. 5 (2012) 7647–7656.
[25] Y. Huang, W. Fan, B. Long, H. Li, F. Zhao, Z. Liu, Y. Tong, H. Ji, Visible light Bi_2S_3/Bi_2O_3/$Bi_2O_2CO_3$ photocatalyst for effective degradation of organic pollutions, Appl. Catal., B 185 (2016) 68–76.
[26] Z. Wang, C. Jiang, R. Huang, H. Peng, X. Tang, Investigation of optical and photocatalytic properties of bismuth nanospheres prepared by a facile thermolysis method, J. Phys. Chem. C 118 (2014) 1155–1160.
[27] Y. Yu, C. Cao, H. Liu, P. Li, F. Wei, Y. Jiang, W. Song, A Bi/BiOCl heterojunction photocatalyst with enhanced electron-hole separation and excellent visible light photodegrading activity, J. Mater. Chem. A 2 (2014) 1677–1681.
[28] F. Dong, Z. Zhao, Y. Sun, Y. Zhang, S. Yan, Z. Wu, An advanced semimetal-organic bi spheres-g-C_3N_4 nanohybrid with SPR-enhanced visible-light photocatalytic performance for NO purification, Environ. Sci. Technol. 49 (2015) 12432–12440.
[29] Z. Zhao, Y. Zhou, F. Wang, K. Zhang, S. Yu, K. Cao, Polyaniline-decorated 001 facets of Bi2O2CO3 nanosheets. in situ oxygen vacancy formation and enhanced visible light photocatalytic activity, ACS Appl. Mater. Inter. 7 (2015) 730–737.
[30] F. Lei, Y. Sun, K. Liu, S. Gao, L. Liang, B. Pan, Y. Xie, Oxygen vacancies confined in ultrathin indium oxide porous sheets for promoted visible-light water splitting, J. Am. Chem. Soc. 136 (2014) 6826–6829.
[31] Y. Lv, W. Yao, R. Zong, Y. Zhu, Fabrication of wide–range–visible photocatalyst Bi_2WO_{6-x} nanoplates via surface oxygen vacancies, Sci. Rep. 6 (2016) 19347.
[32] W. Cui, X. Li, C. Gao, F. Dong, X. Chen, Ternary Ag/AgCl-$(BiO)_2CO_3$ composites as high-performance visible-light plasmonic photocatalysts, Catal. Today 284 (2017) 67–76.
[33] J.C.S. Wu, Y.T. Cheng, *In situ* FTIR study of photocatalytic NO reaction on photocatalysts under UV irradiation, J. Catal. 237 (2006) 393–404.
[34] Y. Zhou, Z. Zhao, F. Wang, K. Cao, D.E. Doronkin, F. Dong, J.D. Grunwaldt, facile synthesis of surface N-doped $Bi_2O_2CO_3$: origin of visible light photocatalytic activity and in situ DRIFTS studies, J. Hazard. Mater. 307 (2016) 163–172.
[35] G. Kim, S.H. Lee, W. Choi, Glucose–TiO_2 charge transfer complex-mediated photocatalysis under visible light, Appl. Catal. B 162 (2015) 463–469.
[36] Y. Zhu, Q. Ling, Y. Liu, H. Wang, Y. Zhu, Photocatalytic performance of $BiPO_4$ nanorods adjusted via defects, Appl. Catal., B 187 (2016) 204–211.
[37] H. Yu, X. Li, X. Quan, S. Chen, Y. Zhang, Effective utilization of visible light (including $\lambda > 600$ nm) in phenol degradation with p-Silicon nanowire/TiO_2core/shell heterojunction array cathode, Environ. Sci. Technol. 43 (2009) 7849–7855.
[38] H. Zhu, X. Chen, Z. Zheng, X. Ke, E. Jaatinen, J. Zhao, C. Guo, T. Xie, D. Wang, Mechanism of supported gold nanoparticles as photocatalysts under ultraviolet and visible light irradiation, Chem. Commun. (2009) 7524–7526.
[39] J. Jiang, L. Zhang, H. Li, W. He, J.J. Yin, Self-doping and surface plasmon modification induced visible light photocatalysis of BiOCl, Nanoscale 5 (2013) 10573–10581.
[40] D. Li, Z. Chen, Y. Chen, W. Li, H. Huang, Y. He, X. Fu, A new route for degradation of volatile organic compounds under visible light: using the bifunctional photocatalyst Pt/$TiO_{2-x}N_x$ in H_2–O_2 atmosphere, Environ. Sci. Technol. 42 (2008) 2130–2135.
[41] X.Z. Li, F.B. Li, Study of Au/Au^{3+}-TiO_2 photocatalysts toward visible photooxidation for water and wastewater treatment, Environ. Sci. Technol. 35 (2001) 2381–2387.
[42] F. Dong, T. Xiong, Y. Sun, Z. Zhao, Y. Zhou, X. Feng, Z. Wu, A semimetal bismuth element as a direct plasmonic photocatalyst, Chem. Commun. 50 (2014) 10386–10389.
[43] X. Hou, X. Huang, F. Jia, Z. Ai, J. Zhao, L. Zhang, Hydroxylamine promoted goethite surface fenton degradation of organic pollutants, Environ. Sci. Technol. 51 (2017) 5118–5126.
[44] Z. Zhu, H. Pan, M. Murugananthan, J. Gong, Y. Zhang, Visible light-driven photocatalytically active g-C_3N_4 material for enhanced generation of H_2O_2, Appl. Catal., B 232 (2018) 19–25.
[45] J. Kim, C.W. Lee, W. Choi, Platinized WO_3 as an environmental photocatalyst that generates OH radicals under visible light, Environ. Sci. Technol. 44 (2010) 6849–6854.
[46] F. Dong, Q. Li, Y. Sun, W.K. Ho, Noble metal-like behavior of plasmonic Bi particles as a cocatalyst deposited on $(BiO)_2CO_3$ microspheres for efficient visible light photocatalysis, ACS Catal. 4 (2014) 4341–4350.